J. COMBIN. MATH. COMBIN. COMPUT. 127a (2025) 4629-4648

Journal of Combinatorial Mathematics and Combinatorial Computing
www.combinatorialpress.com/jcmcc

Numerical simulation study on the damage mechanism of U26Mn2Si2CrNiMo bainitic austenitic withdrawn fork steel by nonmetallic inclusions

Shibo Liu[1,✉], Zhiqing Chen[2]

[1] *School of Materials Science and Engineering, Shenyang Aerospace University, Shenyang, Liaoning, 110000, China*

[2] *School of Management, Chongqing University of Technology, Chongqing, 400054, China*

ABSTRACT

In this paper, for the influence of non-metallic inclusions on the contact fatigue performance of steel, based on the finite element method and rolling contact fatigue theory, the contact fatigue model of U26Mn2Si2CrNiMo bainitic austenitic steel containing non-metallic inclusions is established. The characteristics of non-metallic inclusions and U26Mn2Si2CrNiMo bainitic austenitic steel are analyzed. To investigate the changes in the composition, density and size of each inclusions during the production steps of U26Mn2Si2CrNiMo bainitic austenitic steel by using the inclusions detection technique in steel, the stress and strain response algorithm and the thermodynamic calculations (deoxidization equilibrium calculations of the steel liquid). To analyze the range of fatigue damage concentration caused by non-metallic inclusions by characterizing the distribution of subsurface fatigue damage in the RCF process of U26Mn2Si2CrNiMo bainitic austenitic steel. Explore the effect of the distribution depth of individual non-metallic inclusions on the contact fatigue life of U26Mn2Si2CrNiMo bainitic austenitic steel, and the role of the angle of arrangement of dual non-metallic inclusions on the properties of U26Mn2Si2CrNiMo bainitic austenitic steel. When circular alumina inclusions with a radius of 5 μm are located at different depths of the bainitic austenitic steel, the von Mises stress reaches a maximum value of 770.0 MPa at a depth of 0.53 mm (0.67 b_H) of inclusions, which is increased by 18.5% compared to the case without inclusions (650 MPa). When the spacing of the two inclusions is 2.5 r (12.5 μm) and the depth is 0.5 mm, the arrangement of the nonmetallic inclusions affects the predicted fatigue life, and the two inclusions reduce the predicted fatigue life around them to different degrees.

Keywords: Nonmetallic inclusions, bainitic austenitic steel, rolling contact fatigue, stress-strain response

✉ Corresponding author.
E-mail address: liushibo200010@163.com (S. Liu).
Received 05 February 2024; Revised 12 April 2024; Accepted 05 December 2024; Published Online 15 April 2025.
DOI: 10.61091/jcmcc127a-262

1. Introduction

Non-metallic inclusions in steel are oxides, sulfides, silicates and nitrides in steel that do not have metallic properties [1-2]. They are steel in the smelting process due to the addition of deoxidizers to form oxides, silicates and steel in the solidification process due to the solubility of certain elements (such as sulfur, nitrogen) and the formation of sulfides, nitrides, these inclusions are too late to discharge and remain in the steel [3-6]. Foreign inclusions are slag or refractory materials or other inclusions in the liquid steel solidification process did not surface in time and remain in the steel [7-8]. They are often used as an important indicator of steel quality, its type, composition, morphology, content, size, distribution and other state factors have an impact on steel properties [9-11].

With the development of modern refining technology, steel “cleanliness” greatly improved, the content of inclusions in steel, although very small, but the performance of steel has a non-negligible impact, non-metallic inclusions in steel destroys the continuity of the metal matrix [12-15], resulting in the material's plasticity, toughness and fatigue performance is reduced, so that steel's Cold and hot processing performance and even some physical properties of steel is bad [16-17]. The impact of steel inclusions on steel performance is mainly manifested in the harm to the toughness of steel, and the degree of harm with the increase in the strength of steel and increase. However, the quantity and distribution pattern of inclusions is one of the important indicators of steel quality [18-21]. Therefore, in order to reduce the influence of non-metallic inclusions on steel properties, appropriate process measures and additives, such as deoxygenation, desulfurization and other treatments, will be taken in the steelmaking process in order to improve the quality and properties of steel [22-25].

This paper analyzes the characteristics of the types of non-metallic inclusions and the way to remove them, and characterizes and introduces the chemical composition of U26Mn2Si2CrNiMo bainitic austenitic withdrawal fork steel, the subject of the study. The rolling contact fatigue mechanism is proposed, and rolling contact fatigue experiments are carried out by line contact method to summarize the relevant factors affecting the rolling contact fatigue of the test material. The inclusions detection method is proposed for the steel, and the thermodynamic data of the test steel are selected to calculate the deoxidized equilibrium value of the steel liquid. Set up U26Mn2Si2CrNiMo bainitic austenitic steel production process and smelting program, and analyze the change of inclusions in the production process of bainitic austenitic steel. Set up the RCF model of fatigue damage distribution to analyze the effect of non-metallic inclusions on the fatigue damage of U26Mn2Si2CrNiMo bainitic austenitic steel, as well as the role of single/multiple non-metallic inclusions on the contact fatigue life of U26Mn2Si2CrNiMo bainitic austenitic steel.

2. Experimental basis

2.1. Non-metallic inclusions

As the liquid steel contains oxygen, nitrogen, sulfur and other elements, when the temperature is lowered, the solubility of these elements will also be gradually reduced. Such as in the pouring process, the temperature of the molten steel is gradually reduced, oxygen, nitrogen, sulfur and other elements are gradually precipitated, combined with aluminum, calcium, titanium and other elements in the molten steel to generate oxide inclusions, whose state of existence is generally not affected by the impact of the heat treatment state and change. Inclusions can be divided into endogenous inclusions and foreign inclusions according to their sources, and the sources of inclusions are shown in Figure 1. Endogenous inclusions are steel deoxygenation products or precipitates in the solidification process, foreign inclusions are steel and the outside world mechanical action or accidental chemical reaction products. Usually foreign inclusions are large in size and are easily removed by floating in the steel, but their composition is complex and sporadically distributed in the steel.

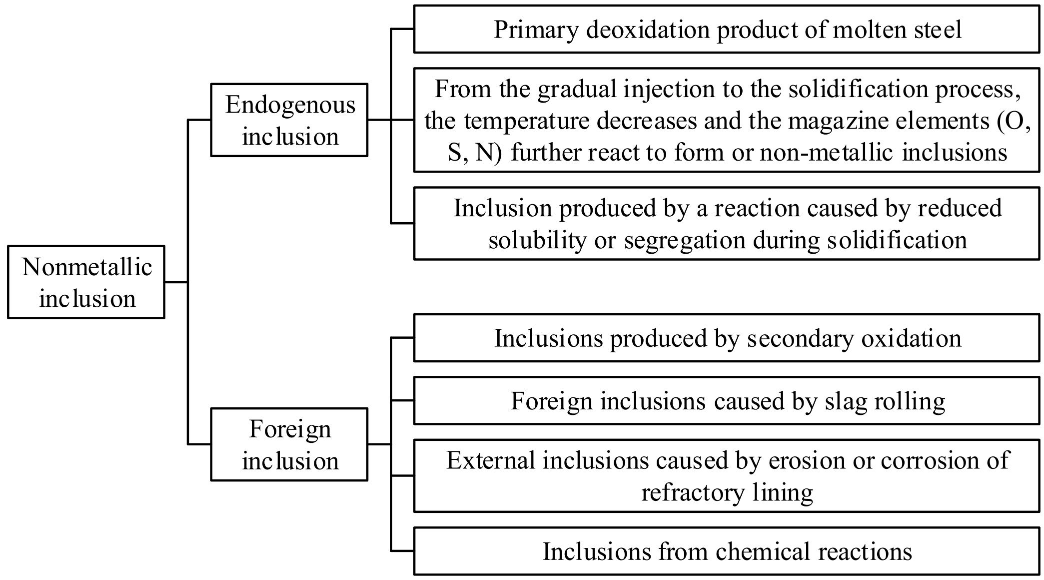

Fig. 1. The source of the inclusion

2.1.1. Types of nonmetallic inclusions Non-metallic inclusions in steel can be categorized differently from different perspectives [26].

1) According to the degree of deformation of inclusions during thermal processing can be divided into: brittle inclusions, plastic inclusions, point-like non-deformation inclusions and semi-plastic inclusions.

2) According to the size of non-metallic inclusions classification

According to the size of inclusions can be divided into: super-microscopic inclusions, microscopic inclusions, macroscopic inclusions, deoxidation product inclusions, foreign inclusions.

3) According to the inclusions of the form and composition classification

According to the different composition, color and morphology of inclusions can be divided into: sulfide (Class A), alumina (Class B), silicate (Class C), spherical oxides (Class D), single-particle spherical class (Class DS).

2.1.2. Removal of non-metallic inclusions. The main way to reduce non-metallic inclusions in steel is to minimize the penetration of foreign inclusions into the steel water. The second is to try to make the inclusions in the steel water to float to remove, in order to purify the steel.

1) External inclusions control. According to the different sources to take matching measures, in the continuous casting process, the use of slag bar and other slag blocking operations to prevent steel slag involved. Use argon and other inert gases for protective casting to prevent secondary oxidation. Use a larger capacity intermediate package, as far as possible to promote the removal of inclusions floating, the use of alkalinity appropriate protective slag and refractory materials that are not easily eroded.

2) Internal inclusions control. The generation of non-metallic inclusions is unavoidable, how to choose the deoxidizer becomes the key factor to reduce the generation of internal inclusions.

2.2. U26Mn2Si2CrNiMo bainitic austenitic withdrawal fork steel

Bainitic steel is mainly used to improve its mechanical properties by optimizing the alloying elements and optimizing the heat treatment process in 2 ways. For U26Mn2Si2CrNiMo bainitic austenitic steel, the strength and toughness of the material are mainly ensured by adding chemical elements such as Si, Mn, Cr, Mo and Ni. Similarly, its chemical composition reduces the Mo content and increases the Si and Mn content. And usually after normalizing with faster cooling rate way (air cooling) can be obtained bainite austenite organization. After normalizing air cooling process for continuous cooling phase change process, the microstructure of the phase composition and content, microstructural features will be affected by the cooling final cooling temperature. It is generally believed that the material is completely austenitized after rapid cooling without tempering, that is, precipitation phase precipitation will not occur.

2.3. *Rolling contact fatigue RCF*

Rolling contact fatigue is a phenomenon in which two materials or workpieces come into contact with each other under cyclic loading and crack propagation occurs at the same time as crack initiation on the contact surface or subsurface [27-28]. When the crack expands to the surface to form pockmarked spalling, shallow spalling, deep spalling, and penetrating cracks leading to fatigue failure phenomenon. Rolling contact fatigue damage commonly occurs on the contact surface of the workpiece. Under contact stress conditions, surface microcracks expand to the interior at a certain angle and produce secondary cracks. The secondary cracks expand to the surface under the action of shear stress, and eventually form spalling pits in the surface layer leading to failure. It is common to classify contact fatigue damage as abrasion, pitting or spalling and fracture, which accumulate in the subsurface layer of the workpiece and lead to changes in its microstructure.

2.3.1. Rolling contact fatigue mechanism. Rolling contact fatigue is the result of long cyclic repetitions under contact loads. When two parts come into contact with each other there is a localized indentation stress on the contact surface called contact stress or Hertz stress. Under contact stress, according to the difference in the original geometrical conditions of the two workpieces at the time of contact. It can usually be classified into two types, one is line contact (rail contact) and the other is point contact (spherical bearing contact).

This paper is a rolling contact fatigue experiment using line contact. According to the theory of line contact, it is assumed that the radii of the two cylinders are R_1 and R_2, respectively, and the length is L. Due to the elastic deformation, it is a line contact before the deformation, and after the deformation, it transforms into a surface contact with a contact area of $2bL$. By further analyzing the theory of elastomechanics, it can be seen that, in the case of semi-elliptic column along the y-axis, the distribution of the contact compressive stress σ_z. σ_z is maximum when the contact is located at the center $(y=0)$ and there:

$$\sigma_z = \sigma_{z\max}\sqrt{1-\frac{y^2}{b^2}} \tag{1}$$

Eq. (1) where b is the contact surface half-width:

$$b = 1.52\sqrt{\frac{F}{EL}\frac{(R_1R_2)}{(R_1+R_2)}} \tag{2}$$

$$\sigma_{z\max} = 0.418\sqrt{\frac{EL}{F}\frac{(R_1+R_2)}{(R_1R_2)}} \tag{3}$$

where E is the combined modulus of elasticity of the two cylinders, which can be obtained from the modulus of elasticity E_1, E_2 of the two cylinders according to Eq. (4):

$$E = \frac{2E_1E_2}{E_1+E_2} \tag{4}$$

Due to the role of the normal force, the contact force at the contact for three-way compressive stress, $\sigma_z, \sigma_x, \sigma_y$ are the main stress, can be obtained from the change rule of the contact depth. In a certain contact depth under the $\sigma_i > \sigma_y > \sigma_x$, when more than this depth is $\sigma_z > \sigma_x > \sigma_y$, corresponding to the maximum shear stress respectively:

$$\tau_{zy45^\circ} = \frac{\sigma_z - \sigma_y}{2} \tag{5}$$

$$\tau_{zx45^\circ} = \frac{\sigma_z - \sigma_x}{2} \tag{6}$$

$$\tau_{yx45^\circ} = \frac{\sigma_y - \sigma_x}{2} \tag{7}$$

It can be seen that the main shear stress τ_{yx45° is at $z = 0.786b$ when $\tau_{yx45^\circ} \approx 0.3\sigma_{z\max}$ is the maximum value. That is to say, when the two cylinders are under contact pressure, the maximum shear stress τ_{yx45° is at the center of contact $(y = 0)$. and from the depth of contact $0.78b$, the direction of 45 ° with the contact surface, but when the two cylinders are not in contact once, τ_{yx45° is zero.

2.3.2. Factors affecting rolling contact fatigue.According to the rolling contact fatigue mechanism and failure form can be seen, the relative relationship between the material yield strength and the surface maximum integrated shear stress is a key factor in determining the fatigue crack sprouting, when the maximum integrated shear stress on the surface exceeds the material yield strength and shear strength, the cracks are generated on the surface to form a numbness spalling. And when the sub-surface integrated shear stress exceeds the shear strength and yield strength, the crack sprouts on the sub-surface to form shallow spalling. Deep spalling mainly occurs in the surface hardening treatment of the workpiece, cracks sprouted in the transition zone to form deep spalling.

Rolling contact fatigue failure of the influencing factors are numerous and complex, such as the workpiece itself, the internal organization of the material uniformity, surface roughness, the size of the contact stress, the lubrication status, the number of experimental revolutions and friction coefficients, etc., on the fatigue failure mechanism is complex to analyze, and therefore usually only one or two of the influencing factors to analyze and study, which is roughly divided into internal factors and external factors:

1） Internal factors:

(1) non-metallic inclusions: non-metallic inclusions in the steel in the contact process and the matrix junction of elastic-plastic deformation is not coordinated easily induced stress concentration and thus the formation of micro-cracks in the edge of the inclusions so that the contact fatigue life is reduced.

(2) Heat treatment organization.

(3) Hardness.

(4) Depth of surface modification layer.

(5) Residual stress.

2） External factors:

(1) Surface roughness: in the process of contact fatigue, the surface roughness will affect the lubrication state and friction factors, thus changing the location of crack initiation and expansion direction, the larger the roughness, the shorter the fatigue life.

(2) Slip rate: Slip rate will directly affect the plastic deformation of the surface layer, the formation of white etching cracks and wear rate and thus affect the contact fatigue life.

(3) Lubrication status: in the fatigue initiation stage of the lubricant to reduce friction to reduce the role of wear, once the fatigue crack formation, the lubricant will promote the expansion of cracks.

(4) Hardness matching: whether the hardness between the two contact rollers is reasonably matched will directly affect the fatigue life.

3. Test materials and methods

3.1. Test materials

The chemical composition of the U26Mn2Si2CrNiMo austenitic bainitic steel material is shown in Table 1. The test material was obtained in the state of forged billet.

Table 1. Chemical composition of test steel (quality score)

C	Si	Mn	Cr	Ni	Cu	Mo	Sn	Sb
0.32	1.75	1.79	1.32	0.54	0.05	0.43	0.0076	0.0065
Ti	Nb	V	Al	N	P	S	As	
0.005	0.0012	0.014	0.107	0.0076	0.013	0.007	0.0061	

3.2. Detection of inclusions in steel

Metallographic specimen preparation method for inclusions detection and tissue observation is consistent, the specific steps are as follows:
1) Firstly, a 12mm×12mm×15mm specimen for inclusions detection was cut on a 15mm-thick cross-section round steel ingot by wire cutting, and the sampling position was 1/4 of the diameter of the round steel ingot.
2) Use $240^{\#}$, $400^{\#}$, $600^{\#}$, $800^{\#}$, $1000^{\#}$, $1200^{\#}$, $1500^{\#}$, $2000^{\#}$ metallographic sandpaper in turn. The observation surface from coarse to fine grinding step by step, and finally use the hair dryer to blow dry moisture.
3) The ground metallographic specimen will be polished to remove scratches.
4) After finishing the polishing, rinse it with water, drop alcohol on the polishing surface and blow dry the water with hair dryer. When observed under an optical microscope, if the polishing surface is free of scratches, water, dirt, polishing pits, the metallographic specimen preparation is complete.
5) Wrap the polished metallographic specimen with degreasing cotton and put it into the drying tower for spare.

3.2.1. Mixture Characterization. HITACHI SU-5000 Field Emission Scanning Electron Microscope was used to observe the morphology of inclusions, and its composition was detected by EDS. SIGMA ZEISS field emission scanning electron microscope and INCA Feature automatic scanning analysis software were used for quantitative inclusions detection and analysis. The lower limit of inclusions was set to 1 μm (only non-metallic inclusions with a size above 1 μm were scanned and detected). The scanning results are the number of inclusions, their size (equivalent circular diameter ECD), the area of individual inclusions, and the mass percentage of the inclusions' constituent elements. Therefore, it is necessary to convert the mass percentage of elements to the mass percentage of oxides, sulfides, carbon and nitrogen compounds, data processing principles are as follows:
1) Only the oxides containing Mg, Al, Ca, sulfides, and carbon nitrides containing Ti and Nb are considered in the composition of inclusions.
2) Converting Mg, Al, Ca to oxides.
3) Express the mass percentage of sulfides in terms of the mass percentage of element S.
4) Converting Ti, Nb to carbonitrides.

In this way, the effect of Mg treatment on the composition, morphology, size, quantity, distribution and other characteristics of non-metallic inclusions is investigated.

3.2.2. Mixture thermodynamic calculation. In order to support the typical inclusions present in the different process test steels during the test, Factsage thermodynamic calculation software was used to calculate the oxide dominant region map in the U26Mn2Si2CrNiMo bainitic austenitic steel system. As well as equilibrium calculations of inclusions and precipitated phase compositions during cooling of the test program (U26Mn2Si2CrNiMo bainitic austenitic steel) at 1600~1000℃.

3.3. Stress and strain response

Under cyclic contact loading conditions, the stress-strain response can be stabilized after a few loading cycles due to the hardening behavior, which is well known as the stabilization phenomenon.

In polycrystalline material modeling, both kinematic and isotropic hardening are considered. The number of loading cycles required to stabilize the stress-strain response depends on the loading level. The evaluation of the steady state can be easily carried out on the basis of the accumulated plastic strain, which is defined as:

Based on the decomposition of the total strain tensor, the elastic and plastic strain tensor can be expressed as:

$$\varepsilon_{ij} = \varepsilon_{ij}^{e} + \varepsilon_{ij}^{p} \tag{8}$$

The yielding of the material is controlled by the von Mises criterion, which can be given as follows:

$$f = J_2(\sigma - X) - k \le 0 \tag{9}$$

where $J_2(\sigma - X)$ is the vonMises equivalent force for the kinematic hardening model, which can be defined as:

$$J_2(\sigma - X) = \sqrt{3/2(S - X)\cdot(S - X)} \tag{10}$$

where X is the back stress tensor, k represents the initial radius of the yield surface, which is equal to the initial yield limit of the bearing material σ_{yx}. S is the deviation part of the stress tensor, which can be expressed as:

$$S_{ij} = \sigma_{ij} + p\delta_{ij}, p = -1/3\sigma_{ii} \tag{11}$$

Thus the evolution of the plastic strain tensor is defined as follows:

$$\dot{\varepsilon}_{ij}^{p} = \frac{\dot{\lambda}\partial f}{\partial \sigma_{ij}} \tag{12}$$

The value of plastic modulus can be determined as:

$$\lambda = \dot{p} = \sqrt{(2/3)\dot{\varepsilon}_{ij}^{p}\dot{\varepsilon}_{ij}^{p}} \tag{13}$$

The equivalent plastic strain is defined as:

$$\bar{\varepsilon}^{p} = \sqrt{(2/3)\varepsilon_{ij}^{p}\varepsilon_{ij}^{p}}, \varepsilon^{p} = \sum_{\alpha}\gamma^{(\alpha)}(s_0^{(\alpha)} \otimes m_0^{(\alpha)}) \tag{14}$$

Therefore, the equivalent ratchet strain is defined as:

$$\bar{\varepsilon}_{ratch}^{p} = \sqrt{(2/3)\varepsilon_{ratch,ij}^{p}\varepsilon_{ratch,ij}^{p}} \tag{15}$$

3.4. Thermodynamic calculations and analysis

3.4.1. Selection of thermodynamic data.The power of FactSage software stems from the rich database it carries. The thermodynamic database has been created to make it possible to perform generalized thermodynamic calculations within the accuracy of experimental data.

The FactSage thermodynamic calculation system is based on Gibbs energy minimization, and the equilibrium module of the software can perform equilibrium calculations for up to 32 elements, 30 non-ideal solution phases and an unlimited number of stoichiometric compounds, as well as equilibrium calculations for composite systems including slag, molten steel, inclusions, refractories and gases, and is suitable for systems with a wide range of components and a wide range of temperatures. It is suitable for systems with multiple components and a wide temperature range.

The first step is the thermodynamic prediction of the deoxygenation mechanism of aluminum-silicon-manganese alloys for a steel solution (U26Mn2Si2CrNiMo bainitic austenitic steel). The precipitation reaction equation for the deoxygenation of alloying element M (Al, Si, Mn) in the liquid steel at the steelmaking temperature (1600°C) to produce deoxygenation products of the form $M_{xO\gamma}$ is given as:

$$x[M]+y[O]=M_xO_y \tag{16}$$

The activity $a_{M_xO_y}=1$ then the equilibrium constant K of the reaction equation can be expressed in equation (17) when a pure oxide is formed in the liquid steel:

$$\lg K=-x\lg f_M-y\lg f_0-x\lg[M]-y\lg[O] \tag{17}$$

In the above equations, a_i (i is M or O) denotes the activity, [M] and [O] denote the mass fraction of the corresponding element, and f_i denotes the activity coefficient of the corresponding element. And a_i can be calculated from the liquid steel temperature and liquid steel composition by Equilib, the equilibrium module of FactSage software, and then the activity coefficients of each element can be determined.

The standard Gibbs free energy can be written as:

$$\Delta G_m^\theta=-RTlnK \tag{18}$$

3.4.2. Equilibrium calculation of liquid steel deoxidation.Thermodynamic calculations are based on the Gibbs free energy minimization principle. U26Mn2Si2CrNiMo the concentration of the remaining elements in the bainitic austenitic steel solution, except Fe, is low, so the steel solution can be assumed to be an ideal solution and follow Henry's law. The group element activity coefficient is chosen as 1% (mass) very dilute solution as the standard state, and the group element activity coefficient and activity calculation formula is given below:

$$\lg f_i=\sum_{j=2}^{n}e_i^j[\%j] \tag{19}$$

$$a_i=f_i\cdot[\%i] \tag{20}$$

where a_i is the activity of element i. f_i is the activity coefficient of element i. e_i^j is the interaction coefficient of element j on element i. $[\%i],[\%j]$ is the mass fraction of element i and element j, respectively.

4. Test results and analysis

4.1. Typical inclusions variations in the production process of bainitic austenitic steels

4.1.1. Pilot program.U26Mn2Si2CrNiMo bainitic austenitic steel production process is:

KR iron pretreatment → 180t top and bottom re-blowing converter → one 180tLF → double 180tLF → VD → large-sized billet continuous casting (280mm * 380mm) → casting slow cooling → rolling.

For the smelting process of U26Mn2Si2CrNiMo bainitic austenitic steel, the following sampling program was developed:

LF refining were sampled in the primary LF slag, primary LF after alloying, secondary LF inbound, secondary LF after alloying, VD refining were sampled in the VD breaking air, VD soft blowing 10min and 30min, VD outbound, continuous casting in the middle of the casting, billet in the billet in the inner arc of the 1/4 sampling, rolling were sampled in the rail rail head, rail waist, bottom of the rail.

The taken specimens were processed and Aspex automatic scanning electron microscope was used to observe the composition, morphology and size of inclusions. The oxygen and nitrogen content of the steel was analyzed by TCH600 oxygen and nitrogen analyzer, and the content of Ca, Al_s and Mg elements in the steel was detected by ICP. Through the oxygen and nitrogen analysis of the specimen, the analysis of the steel liquid composition and the analysis of non-metallic inclusions, the change rule of typical inclusions in the smelting process of bainitic steel was studied.

4.1.2. Changes in the composition of the mixture.After a LF slag, inclusions are type $CaO-SiO_2-Al_2O_3$ inclusions, inclusions basically do not contain MgO. Combined with the oxygen and nitrogen analysis and the analysis of the composition of the steel, alloy, deoxidizer and white ash brought into the Ca, Al_s is the main reason for this result. Ca, Al_s and steel oxygen or oxide reaction, generating a large number of CaO and Al_2O_3.

After primary LF alloying, the inclusions are type $CaO-SiO_2-Al_2O_3-MgO$ inclusions. Inclusions in the CaO and MgO content increases, Al_2O_3 content decreases, CaO and MgO increase is the result of the reaction of steel slag or liquid steel and refractory reaction. Steel Ca, Al_s and ladle refractory role, erosion of the furnace lining to increase the content of MgO, while Ca, Al_s content decreases, the generation of CaO and Al_2O_3 and other reaction products, Al_2O_3 content decreases because of further reaction with the refractory material in the MgO to generate $CaO-Al_2O_3-MgO$ -type inclusions.

The change of inclusions composition is shown in Fig. 2, in which a, b and c are intermediate package, bloom and rolling material respectively. 1-15 are 150kg of calcium carbide, 200kg of calcium barium silicate/ 150kg of fluorite ball/ 500kg of white ash, 2500kg of iron, 300kg of ferrosilicon/ 300kg of silicomanganese, 100kg of nickel plate, 90kg of molybdenum plate, 100kg of calcium carbide/ 150kg of low-aluminum ferrosilicon, 150kg of vacuum, air breaking, soft blowing for 10min, out of station, open casting, mid-casting, end of casting. 150kg, vacuum, broken air, soft blowing 10min, soft blowing 30min, out of the station, open pouring, mid-pouring, end of pouring.

From the figure, it can be seen from the casting billet to the rail inclusions have undergone a significant transformation, MgO and Al_2O_3 content increased, SiO_2 and CaO content decreased. The distribution of inclusions shows that a certain proportion of magnesium-aluminum spinel inclusions appeared in the rails, corresponding to the decrease in the content of Al_s and Mg in the steel, which is judged to be caused by the transformation of inclusions during the cooling process.

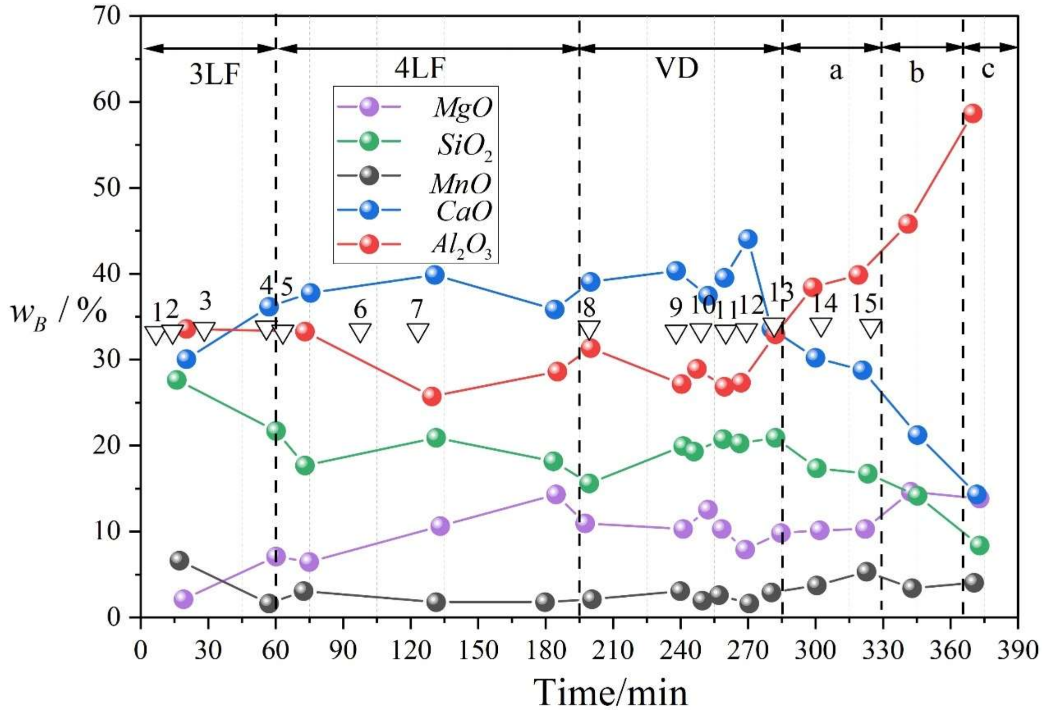

Fig. 2. Changes in inclusion composition

4.1.3. Mixture number density and size change.U26Mn2Si2CrNiMo bainitic austenitic rail typical inclusions surface scanning shows that the rolling process of magnesium-aluminum spinel $CaO-SiO_2-Al_2O_3-MgO$ inclusions occur brittle broken in a chain-like distribution, the inclusions are prone to cause flaw detection failure, endangering the performance of steel rails.

Inclusions number density and average size changes as shown in Figure 3, Figure a, b, c are intermediate package, big square billet, rolled material. 1-15 were 150kg of calcium carbide, calcium barium silicate 200kg / fluorspar ball 150kg / 500kg of white ash, iron 2500kg, ferrosilicon 200kg / silicomanganese 200kg, nickel plate 100kg, molybdenum plate 90kg, calcium barium silicate 100kg / 150kg of low aluminum ferrosilicon, vacuuming, air-breaking, soft blowing for 10min, soft blowing for 30min, out of the station, open pouring, mid-pouring, end of pouring. The graph shows that the number density of non-metallic inclusions in steel has a decreasing trend, and the effect of inclusions removal is remarkable.

After a LF slag number density of inclusions is about 45/ mm^2. With the smelting process, the number of inclusions density continues to decline, including the addition of nickel plate large argon gas stirring steel slag intense reaction inclusions number density increased. vd broken air and soft blowing after about 5/ mm^2, intermediate packages of inclusions number density slightly increased, billet inclusions in the number of density of about 3/ mm^2, with the casting process of inclusions gathered on the removal of the uplift. Due to the influence of rolling, the density of inclusions in the rail increased slightly, about 4 / mm^2. Figure also shows that the average size of inclusions changes, LF and VD stage, due to liquid steel stirring and soft blowing to promote inclusions collision growth uplift removal, inclusions number of density decreases, but the size of the increase in the casting process due to inclusions aggregated uplift, resulting in casting billet inclusions increase in size. Rolling process due to some of the spinel $CaO-SiO_2-Al_2O_3-MgO$ inclusions brittle fracture, resulting in a reduction in the average size of inclusions, the number of slightly increased.

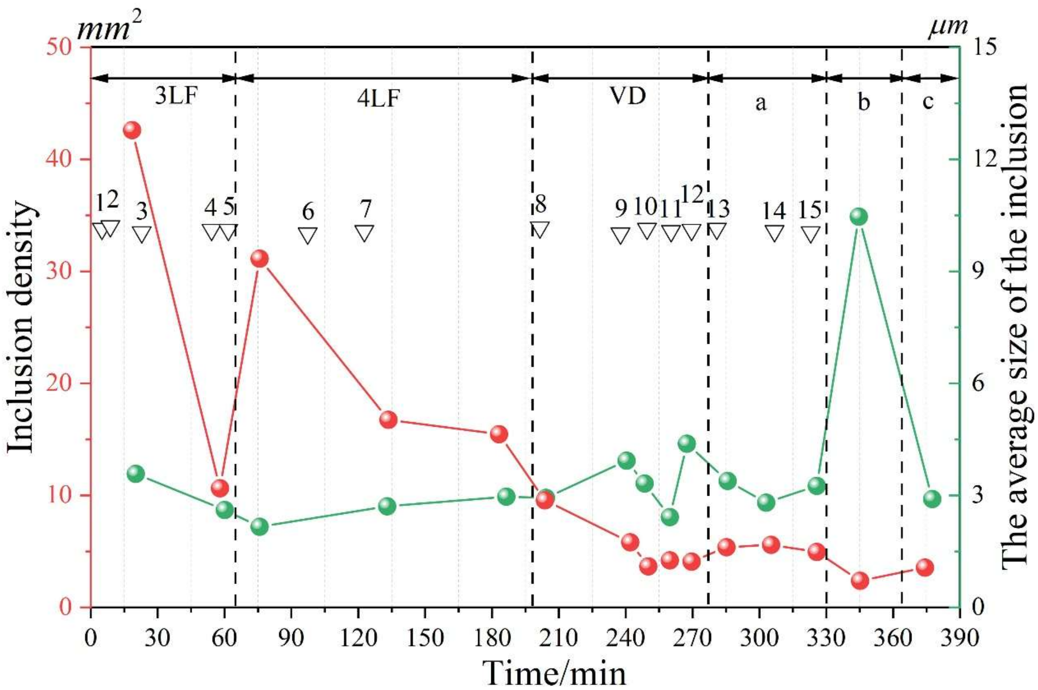

Fig. 3. The density of inclusion and the average size change

4.2. *Quantitative effect of the size of the mixture on fatigue damage*

By characterizing the distribution of subsurface fatigue damage in the RCF process of U26Mn2Si2CrNiMo bainitic austenitic steel, it is possible to further quantitatively characterize the specific values of fatigue damage within the fatigue damage concentration range. In this way, the quantitative analysis of fatigue damage of U26Mn2Si2CrNiMo bainitic austenitic steel by the size of non-metallic inclusions can be clarified. However, the different mesh sizes for different sizes of inclusions result in different volumes of unit nodes in the model for different sizes of inclusions. And the result output of Abaqus for a single structural cell is averaged by the node data within the cell volume. So in order to quantitatively characterize the fatigue damage during RCF, the unit nodes within a certain volume need to be processed by the volume averaging method. Here, the grain corresponding to the cell with the largest subsurface fatigue damage is selected. Since the grain size is uniform, the average fatigue damage $D_{f,ave}$ within this grain by volume averaging can be expressed as:

$$D_{f,ave} = \left[\frac{1}{\sum_{i=1}^{N_E} V_i} \cdot \sum_{i=1}^{N_E} D_{f,i} V_i \right] \tag{21}$$

Where i is the identification number of the unit in the polycrystalline region. N_E is the number of units in the polycrystalline region. V_i is the volume of the target unit. $D_{f,i}$ is the fatigue damage value of the target unit.

4.2.1. Model parameters.For the modeling of inclusions of different sizes, three different sizes of spherical Al_2O_3 inclusions with diameters of 10 μm, 30 μm, and 50 μm were added to the microstructure-sensitive model of polycrystalline materials with reference to the RCF model of fatigue damage distribution proposed in the previous section. In order to prevent the remaining variables from influencing the results, the parameters such as the positions of inclusions and the elastic constants of inclusions in the three models were kept consistent with those in the table, and the

Hertzian contact loads in the models were similarly carried out for 10 cycles. The main parameters in the fatigue crack source prediction model are shown in Table 2.

Table 2. The main parameters in the fatigue crack source prediction model

Parameters	Value	Parameters	Value
Steel matrix, (MPa)	$C_{11} = 302154$ $C_{12} = 135267$ $C_{45} = 95663$	Diameter of inclusions, $d(\mu m)$	50
Young's modulus of inclusions, E (MPa)	404633	Depth to the inclusions, $h(\mu m)$	500
Poisson's ratio of inclusions, v_2	0.32	Radius of cylinder, R (mm)	4.50
Load magnitude, F (kN)	6	/	/

4.2.2. Impact analysis.The equivalent plastic strains of the microstructure-sensitive model with nonmetallic inclusions of sizes 10 μm, 25 μm, and 50 μm, respectively, during 10 cycles of RCF Hertzian contact loading are shown in Fig. 4. The blue solid line in the figure represents the variation of the equivalent plastic strain ε_p and the green solid line represents the variation of the local Mises stress.

The variation of residual stresses and equivalent plastic strains in the steel matrix around inclusions of different sizes during the RCF process shows that the residual stresses and equivalent plastic strains in the steel matrix around inclusions increase with the increase in inclusions size for the same physical parameters, shape, distance from the subsurface location, and applied loads.

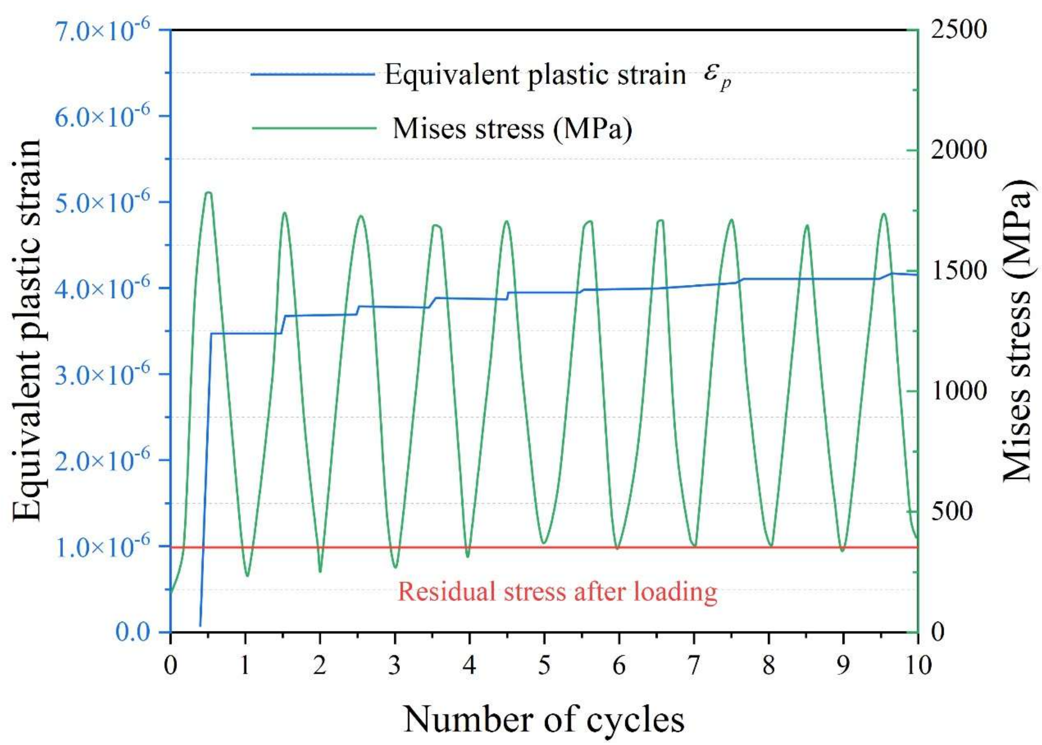

(a) 10 μm inclusion

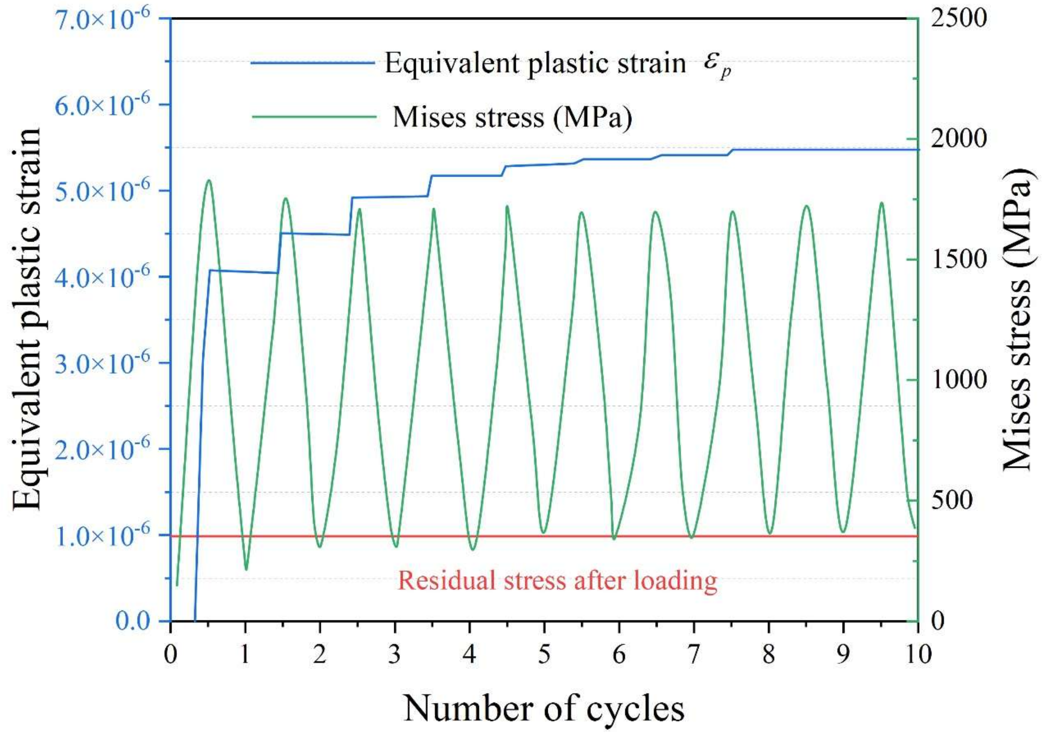

(b) 25 μm inclusion

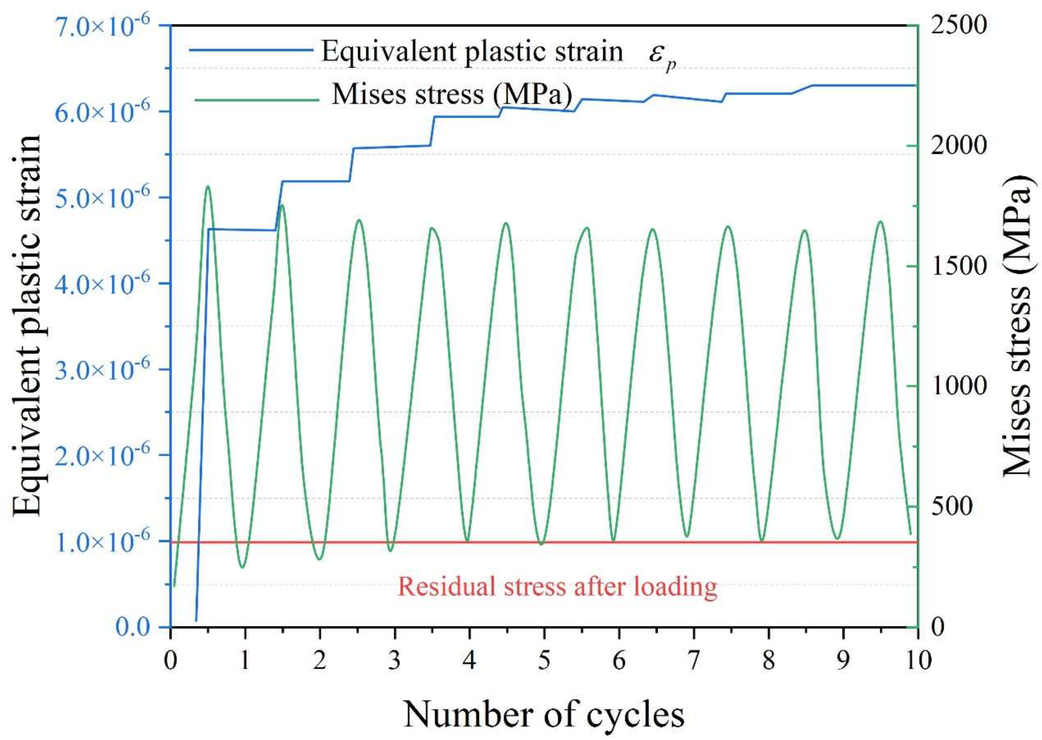

(c) 50 μm inclusion

Fig. 4. Strain changes of steel matrix around different dimensions in the RCF process

The changes of local stress and fatigue damage D_f in the model with the loading cycles in the RCF process are shown in Fig. 5, where the blue solid line represents the changes of equivalent plastic strain D_f and the green solid line represents the changes of local Mises stress.

Through the changes of residual stress and fatigue damage in the steel matrix around inclusions of different sizes during the RCF process, it can be seen that with the larger size of the nonmetallic inclusions, the local fatigue damage in the steel matrix around the inclusions is larger. And since the fatigue damage D_f is set in the subroutine to occur only after each cycle in the cumulative iteration, the slope of the fatigue damage D_f increase within a single cycle is not exhibited in the figure.

At the beginning of the first cycle, the local Mises stresses do not grow from the 0 scale at the beginning truncation of the appearance of the Hertzian contact loads due to the proximity of the location of the initial addition of the Hertzian contact loads to the location of the inclusions. Since RCF fatigue is a multiaxial fatigue controlled by nonconformal Hertzian contact, the angle between the direction of the applied load and the normal cross section of the inclusions varies with the increase of time, so in the first half of the first cycle, the rate of increase of the local Mises stresses shows a trend of increasing and then decreasing, and the same trend is also shown in the second half of the reduction process, and the same trend is also shown in the subsequent process due to the polycrystalline material is subjected to force In the subsequent process, due to the plastic deformation of polycrystalline material after the force, resulting in the accumulation of residual stress after each cycle, while plastic deformation leads to the hardening of the material, resulting in the increment of local residual stress decreases with the increase of cycle times.

At the same time, the initial strength of the slip system of polycrystalline materials is relatively low due to the action of applied load for the first time. The local plastic strain ε_p and fatigue damage D_f increase rapidly due to the microplastic deformation occurring as a result of the applied load. At the same time, due to the presence of the nonlinear hardening criterion in the model, the strength of the polycrystalline material slip system becomes higher and higher, and the critical back stress required for slip opening rises. At the same time, the local plastic strain ε_p and fatigue damage D_f will change less and less until they converge to the fatigue damage at fatigue failure under constant applied loads.

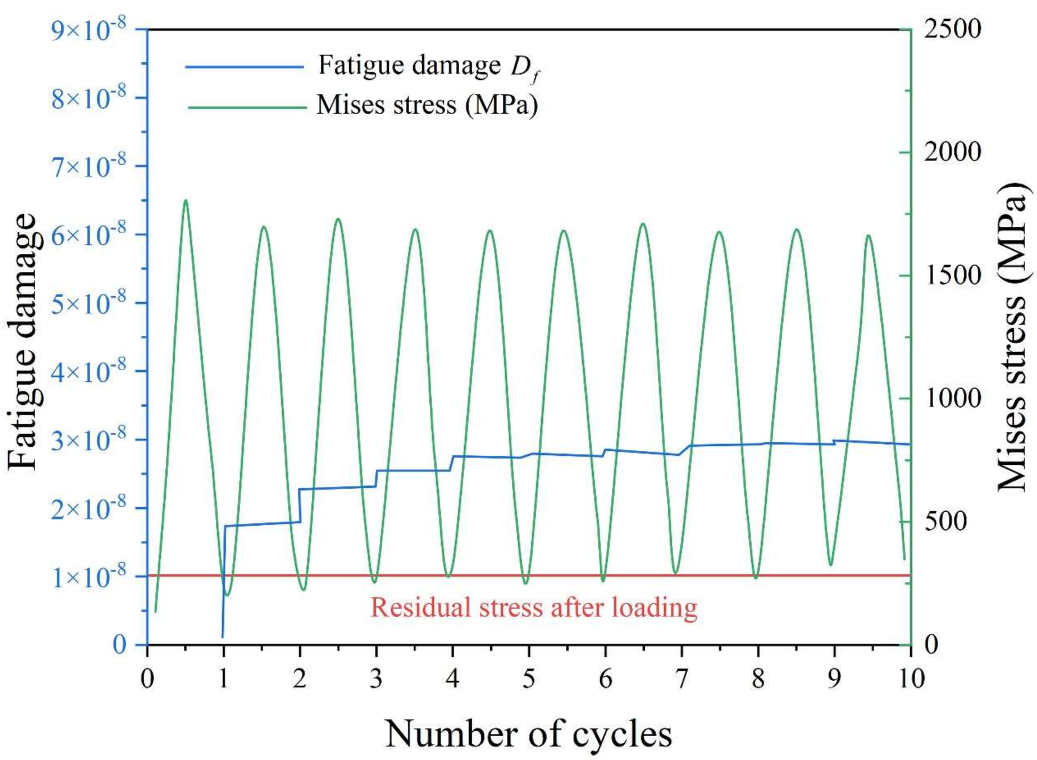

(a) 10 μm inclusion

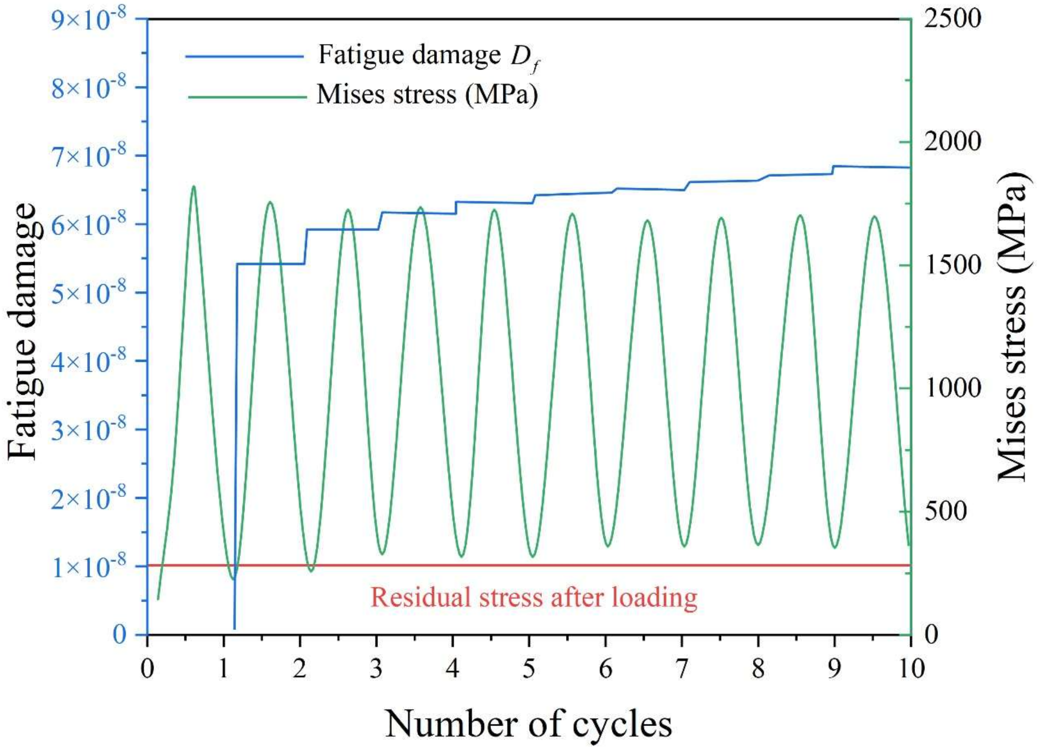

(b) 25 μm inclusion

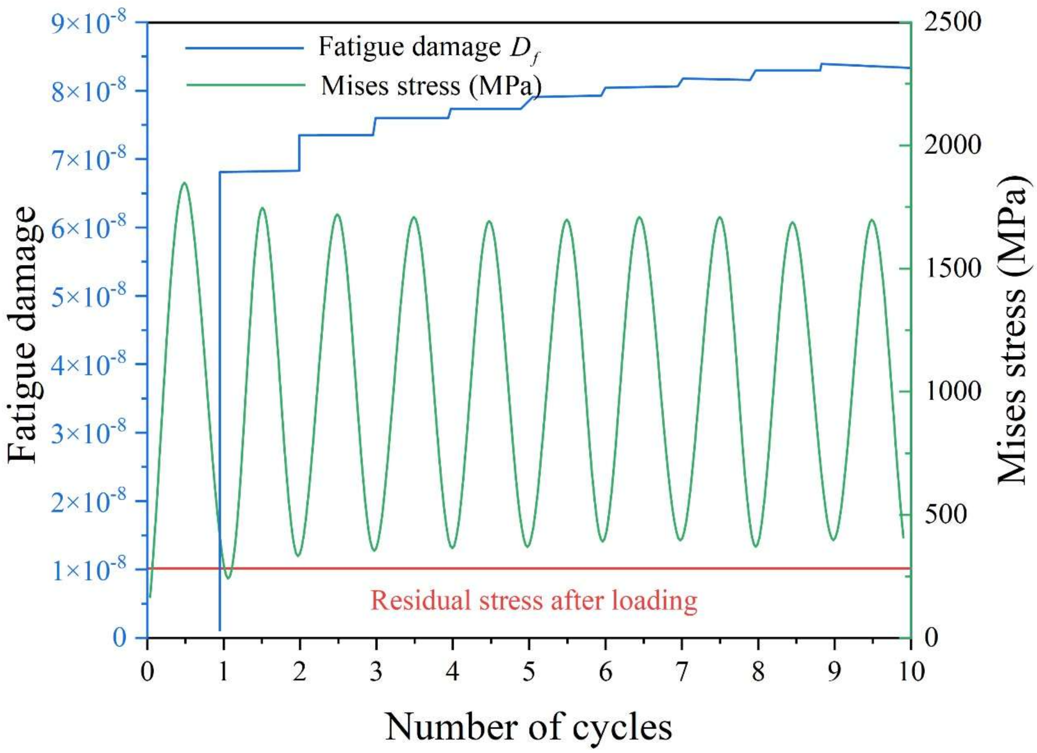

(c) 50 μm inclusion

Fig. 5. Residual stress and fatigue damage change

4.3. Effect of the properties and distribution characteristics of the mixture on the contact fatigue life of steel

4.3.1. The effect of the depth of distribution of inclusions.U26Mn2Si2CrNiMo bainitic austenitic steel has a very complex secondary surface stress field that varies dramatically along the depth direction. Therefore, when the nonmetallic inclusions are located at different depths, they are bound to have different effects on the fatigue life of the bainitic austenitic steel. In this paper, non-metallic individual inclusions are set at different depths on the subsurface, and a contact finite element model of bainitic austenitic steel is established to investigate the effect of the depth of inclusions on the contact fatigue performance of U26Mn2Si2CrNiMo bainitic austenitic steel.

The effect of the depth of non-metallic inclusions on the local maximum stress and predicted fatigue life is shown in Figure 6.

The figure shows the variation of the maximum stress values on the matrix around the inclusions and the minimum predicted fatigue life when circular alumina inclusions with radius 5 μm are located at different depths in bainitic austenitic steel. It can be found that both stresses show a tendency to increase and then decrease with increasing inclusions depth, but the maximum orthogonal shear stress reaches its maximum value at a relatively shallower inclusions depth. Among them, the von Mises stress reaches its maximum value of 770.0 MPa at an inclusions depth of 0.53 mm (0.67 b_H), which is 18.5% larger compared to the case without inclusions (650 MPa). The orthogonal shear stress amplitude, on the other hand, reaches a maximum value of 648 MPa at 0.41 mm (0.49 b_H), which is a 15.1% increase compared to the case without inclusions (563 MPa).

In contrast to the stress trend, the predicted fatigue life on the matrix around the inclusions decreases and then increases with depth. There is a minimum value of $10^{8.50}$ at 0.4 mm (0.49 b_H) for inclusions, which is smaller than $10^{9.13}$ for the case without inclusions.

Both fatigue life and shear stress reach their minimum or maximum values at a depth of about 0.49 b_H, which indicates that non-metallic inclusions have the highest shear stress and the lowest fatigue life at this depth.

Although the Morrow-Brown-Miller multiaxial stress criterion was used to consider the multiaxial stress characteristics, the location of the depth of failure due to nonmetallic inclusions shows a great correlation with the location of the depth of maximum shear stress. It indicates that the fatigue failure mode caused by nonmetallic inclusions is highly correlated with shear action.

Where the red horizontal solid line is the size of the minimum fatigue life on the substrate when there are no inclusions $10^{9.13}$ cycle. It can be found that the localized minimum fatigue life on the matrix around the nonmetallic inclusions is less than $10^{9.13}$ cycles when the depth of the nonmetallic inclusions is from 0.21 mm to 0.84 mm (0.21 b_H -1.05 b_H). It can be regarded that non-metallic inclusions at a depth of 0.21b b_H to 1.05 b_H have an effect on the contact fatigue properties of this bainitic austenitic steel. When the depth of non-metallic inclusions is less than 0.21 b_H or more than 1.05 b_H, the presence of non-metallic inclusions does not affect the contact fatigue performance of the bainitic austenitic steel.

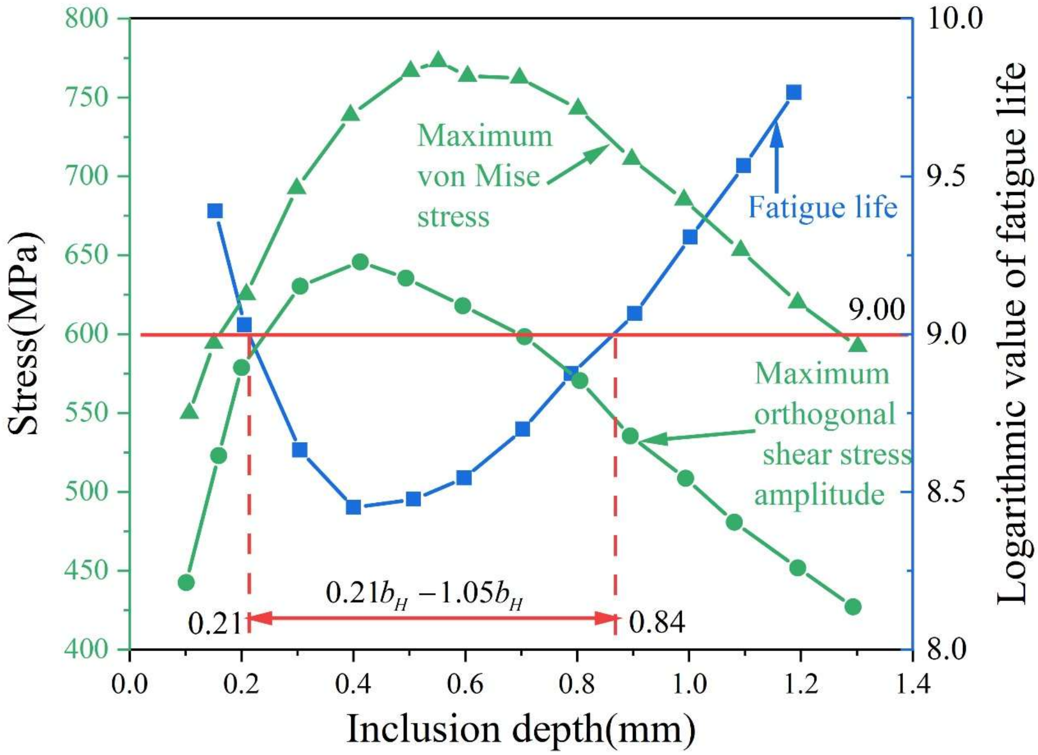

Fig. 6. The effect of inclusion depth on stress and fatigue life

4.3.2. Effect of the angle of alignment of double inclusions.When two inclusions are in close proximity, the stress field on the substrate around them is significantly different from that at a single inclusion. The stress field around the two inclusions interacts with each other, causing a redistribution of stresses.

In general, the two inclusions cause a larger maximum stress and a larger area of high stress region than in the case of a single inclusions. Accordingly, the predicted fatigue life obtained is reduced to varying degrees compared to the case of a single inclusions.

The effect of the alignment angle of non-metallic inclusions on the stress and predicted fatigue life is shown in Fig. 7, which demonstrates the variation of the maximum stress and predicted fatigue life on the substrate around the inclusions when the depth of the inclusions is 0.5 mm and the spacing of the two inclusions (the distance between the centers of the two inclusions) is 2.5 r (12.5 μm), along with the variation of the alignment angle φ.

It can be noticed that the predicted fatigue life around the nonmetallic inclusions decreases to varying degrees due to the alignment of the inclusions. As the angle φ varies, the von Mises stress increases and then decreases, showing symmetry on the 90° axis. φ The maximum von Mises stress remained almost unchanged when varying from 0 to 30° and from 150° to 180°. φ When varying from 60° to 120°, the maximum von Mises stress increases substantially.

The maximum orthogonal shear stress amplitude showed cyclic fluctuations, with φ at higher levels at 30°, 60°, 120°, and 150°. The predicted fatigue life is lower at 30° to 45° and 120° to 150°.

It is clear that the predicted fatigue life is affected by the combination of von Mises stresses as well as shear stresses. The maximum von Mises stress and the maximum orthogonal shear stress amplitude are at lower levels when φ=0 or 180°, i.e., when the two inclusions are parallel to the rolling direction. Therefore, the calculated predicted fatigue life is also at a higher level.

The fatigue failure mode caused by non-metallic inclusions is highly correlated with the shear stresses, so when φ= 90° or so, i.e., when the non-metallic is approximately perpendicular to the rolling direction, the von Mises stresses are at a high level, but because the shear stresses are at a high level, the corresponding predicted fatigue life obtained at this time is also very low.

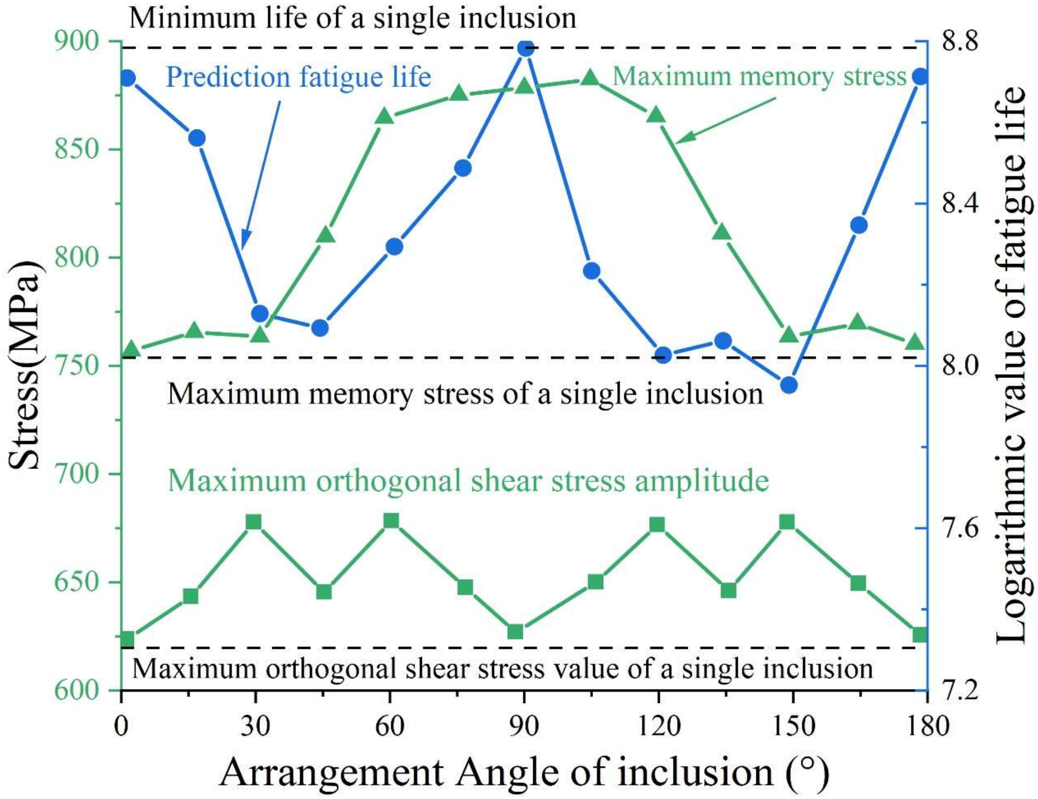

Fig. 7. The influence of the arrangement Angle and the prediction fatigue life

5. Conclusion

This paper focuses on analyzing the effect of non-metallic inclusions on the fatigue damage of U26Mn2Si2CrNiMo bainitic austenitic steel. It focuses on the changes of non-metallic inclusions in the production of U26Mn2Si2CrNiMo bainitic austenitic steel and the effects of non-metallic inclusions on the properties of U26Mn2Si2CrNiMo bainitic austenitic steel.

1) The production of U26Mn2Si2CrNiMo bainitic austenitic steel requires strict control of ferrosilicon and calcium barium silicate in the Al_s, as well as the content of other impurities in the auxiliary materials, which play an important role in the improvement of the typical inclusions in bainitic steel.

2) Establish a RCF process model for bainitic austenitic steels to quantitatively characterize the values of fatigue damage caused by nonmetallic inclusions.The residual stresses and equivalent plastic strains in the steel matrix around the inclusions increase with the increase in the size of the inclusions in the process of 10 cycles of RCF Hertzian contact loading with the same other condition parameters.

3) The contact finite element model of bainitic austenitic steel is established, and circular alumina inclusions with a radius of 5 μm are set at different depths on the subsurface, and the maximum von Mises stress and the maximum orthogonal shear stress amplitude of the two kinds of stresses show a tendency to increase and then decrease with the increase of the depth of the inclusions, but the depth of the inclusions at which the maximum orthogonal shear stress reaches its maximum value is relatively shallower.

The predicted fatigue life around the nonmetallic inclusions decreases to varying degrees when the depth is 0.5 mm and the spacing between the two inclusions is 2.5 r (12.5 μm). As the angle φ varied, the von Mises stresses first increased and then decreased, showing symmetry on a 90° axis.

References

[1] Kazakov, A. A., & Zhitenev, A. I. (2018). Assessment and interpretation of nonmetallic inclusions in steel.

CIS Iron Steel Rev, 16(2), 33-38.

[2] Yang, W., Peng, K., Zhang, L., & Ren, Q. (2020). Deformation and fracture of non-metallic inclusions in steel at different temperatures. Journal of Materials Research and Technology, 9(6), 15016-15022.

[3] Park, J. H., & Kang, Y. (2017). Inclusions in stainless steels– a review. steel research international, 88(12), 1700130.

[4] Liu, H., Zhang, S., Zhang, J., Ren, Q., Zhang, L., & Ge, Y. (2023). Properties of typical non-metallic inclusions in steel: First-principles calculations. Materials Today Communications, 34, 105118.

[5] Zhang, L., Ren, Q., Duan, H., Ren, Y., Chen, W., Cheng, G., ... & Sridhar, S. (2020). Modelling of non-metallic inclusions in steel. Mineral Processing and Extractive Metallurgy, 129(2), 184-206.

[6] Ånmark, N., Karasev, A., & Jönsson, P. G. (2015). The effect of different non-metallic inclusions on the machinability of steels. Materials, 8(2), 751-783.

[7] Wang, J., Liu, W., Yang, S., Liu, Q., Qi, Z., & Li, J. (2024). Evolution and Multidimensional Characterization of Non-metallic Inclusions in Steel: An Industrial Study. JOM, 1-16.

[8] Chen, C., Jiang, Z., Li, Y., Zheng, L., Huang, X., Yang, G., ... & Li, H. (2019). State of the art in the control of inclusions in tire cord steels and saw wire steels–A Review. steel research international, 90(8), 1800547.

[9] Gupta, A., Goyal, S., Padmanabhan, K. A., & Singh, A. K. (2015). Inclusions in steel: micro–macro modelling approach to analyse the effects of inclusions on the properties of steel. The International Journal of Advanced Manufacturing Technology, 77, 565-572.

[10] Wang, L., Yang, S., Li, J., Zhang, S., & Ju, J. (2017). Effect of Mg addition on the refinement and homogenized distribution of inclusions in steel with different Al contents. Metallurgical and Materials Transactions B, 48, 805-818.

[11] Shi, W. N., Yang, S. F., & Li, J. S. (2021). Effect of nonmetallic inclusions on localized corrosion of spring steel. International Journal of Minerals, Metallurgy and Materials, 28, 390-397.

[12] Steneholm, K., Andersson, N. A. I., Tilliander, A., & Jönsson, P. G. (2018). The role of process control on the steel cleanliness. Ironmaking & Steelmaking, 45(2), 114-124.

[13] Bul'ko, B., Molnár, M., Demeter, P., Baricová, D., Pribulová, A., & Futáš, P. (2018). Study of the Influence of intermix conditions on steel cleanliness. Metals, 8(10), 852.

[14] Wang, P., Wang, B., Liu, Y., Zhang, P., Luan, Y. K., Li, D. Z., & Zhang, Z. F. (2022). Effects of inclusion types on the high-cycle fatigue properties of high-strength steel. Scripta Materialia, 206, 114232.

[15] Tervo, H., Kaijalainen, A., Pikkarainen, T., Mehtonen, S., & Porter, D. (2017). Effect of impurity level and inclusions on the ductility and toughness of an ultra-high-strength steel. Materials Science and Engineering: A, 697, 184-193.

[16] Wang, Y., Karasev, A., Park, J. H., & Jönsson, P. G. (2021). Non-metallic inclusions in different ferroalloys and their effect on the steel quality: A review. Metallurgical and Materials Transactions B, 52, 2892-2925.

[17] Li, M., Wu, H., & Sun, Y. (2022). Effect of the inclusion features on mechanical properties of steel. Ironmaking & Steelmaking, 49(4), 405-411.

[18] Wang, X., Wu, Z., Li, B., Chen, W., Zhang, J., & Mao, J. (2024). Inclusions modification by rare earth in steel and the resulting properties: A review. Journal of Rare Earths, 42(3), 431-445.

[19] Yang, C., Luan, Y., Li, D., & Li, Y. (2019). Effects of rare earth elements on inclusions and impact toughness of high-carbon chromium bearing steel. Journal of Materials Science & Technology, 35(7), 1298-1308.

[20] Zhang, C. J., Gao, L. N., & Zhu, L. G. (2018). Effect of inclusion size and type on the nucleation of acicular ferrite in high strength ship plate steel. ISIJ International, 58(5), 965-969.

[21] Zhou, C., Liu, X., Zhang, Y., Wu, H., & Yang, Y. (2022). Numerical study on effect of inclusions on hydrogen segregation in steel under stress conditions. International Journal of Hydrogen Energy, 47(46), 20310-20322.

[22] Gorkusha, D., Karasev, A. V., Komolova, O., Grigorovich, K. V., & Jönsson, P. G. (2020). Characterization of non-metallic inclusions and clusters during production of low-carbon if steel. ISIJ International, 60(12), 2819-2828.

[23] ZHU, M., & DENG, Z. (2021). Evolution and control of non-metallic inclusions in steel during secondary refining process. Acta Metall Sin, 58(1), 28-44.

[24] Wang, Y., Karasev, A., & Jönsson, P. G. (2019). An investigation of non-metallic inclusions in different ferroalloys using electrolytic extraction. Metals, 9(6), 687.

[25] Qiu, G., Zhang, H., Gao, P., Li, R., Wang, G., & Cao, L. (2024). Research progress of desulfurization refining slag: a review. steel research international, 95(1), 2300333.

[26] Aristotel Issagulov,Pavel Kovalev,Sergey Melnik,Vitaliy Kulikov,Svetlana Kvon & Saniya Arinova. (2024). The effect of complex extra-furnace treatment of metal melts on the formation of non-metallic inclusions in large-sized ingots. Materials Research Express(11),116502-116502.

[27] Xue Li,Yuexin Wang,Gao Pu & Kaiyun Wang. (2024). Research on the Wheel Wear and Rolling Contact Fatigue of Metro Vehicle Induced by Rail Corrugation. Tribology Transactions(6),1168-1179.

[28] JianChen,YilongLiang,ShaolongLi,MingYang & YuguanSun. (2024). Rolling Contact Fatigue Behaviors of 20CrNi2Mo Steel by a New Carbon and Nitrogen Composite Infiltration Process. Fatigue & Fracture of Engineering Materials & Structures(1),296-311.